

# Tactile-based Exploration, Mapping and Navigation with Collision-Resilient Aerial Vehicles

Karishma Patnaik, Aravind Adhith Pandian Saravanakumaran and Wenlong Zhang\*

**Abstract**—This article introduces XPLORER, a passive deformable quadrotor UAV with a spring-augmented chassis and proprioceptive state awareness, designed to endure collisions and maintain smooth contact with the environment. A fast-converging external force estimation algorithm for XPLORER is designed to leverage onboard sensors and proprioceptive data for contact detection. Using this force information, four motion primitives are proposed, including three novel tactile-based primitives—tactile-traversal, tactile-turning, and ricocheting—to aid XPLORER in navigating unknown environments. These primitives are synthesized autonomously in real time to enable efficient exploration and navigation by leveraging collisions and contacts. Experimental results demonstrate the effectiveness of our approach, highlighting the potential of *passive* deformable UAVs for contact-rich real-world tasks such as non-destructive inspection, surveillance and mapping, and pursuit/evasion.

## I. INTRODUCTION

Conventional multirotor unmanned aerial vehicles (UAVs), often rely on external attachments or complex actuation mechanisms for tasks such as grasping, perching, or pushing/pulling [1]–[6]. While reconfigurable UAVs offer improved flight efficiency over rigid designs, they still rely on prior knowledge of the environment [7]–[10]. These platforms often struggle to operate autonomously in cluttered, unstructured environments—such as during search and rescue, disaster response and pursuit/evasion—where contact with unknown surfaces is inevitable. Limited compliance makes such UAVs vulnerable to unpredictable behaviors upon collision, such as bouncing, instability, or complete mission failure. This severely constrains their ability to safely navigate confined spaces or adapt to complex surface geometries [11].

In contrast, passive deformable UAVs adapt their morphology naturally in response to contact forces, using springs, origami structures, or soft bodies to absorb impact energy and retain stability [12]–[15]. This article advances the scope of passive deformable UAVs by introducing new tactile-based planning and control algorithms for reliable performance in demanding real-world scenarios.

### A. Related Literature

1) *External Wrench Estimation*: Augmenting a UAV with force-torque sensors is the most common approach to detect external wrench, but it increases the total weight of the UAV and adversely affects flight time [16], [17]. Alternatively,

This material is based upon work supported by the National Science Foundation under Grant No. 2331781.

The authors are with School of Manufacturing Systems and Networks, Ira A. Fulton Schools of Engineering, Arizona State University, Mesa, AZ, 85212, USA. Email: {kpatnaik, apandian, wenlong.zhang}@asu.edu.

\*Address all correspondence to this author.

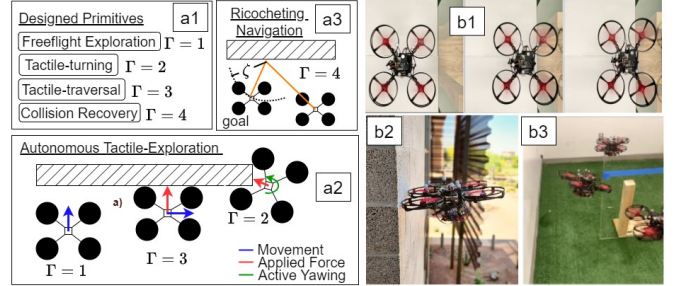


Fig. 1. An overview of the article. (a1) The four primitives ( $\Gamma$ ) proposed to facilitate autonomous missions with deformable UAVs. (a2)–(a3) Automatic online synthesis of  $\Gamma$  for tactile-based exploration and navigation. (b1) Sequence of slow-motion snapshots highlighting the chassis deformation upon contact. (b2) XPLORER enables tactile-based mapping of buildings using (a2). (b3) Ricocheting for agile maneuvering using (a3).

researchers have developed algorithms based on momentum-based [18], [19] and acceleration-based [20], [21] wrench estimators which rely on the available onboard sensors only such as inertial measurement units (IMUs). Kalman filtering approaches and hybrid methods, fusing momentum and acceleration-based wrenches, were proposed in [22], [23] for conventional UAVs. For this work, we aim to exploit *proprioceptive* information about the vehicle’s morphology to improve the force estimate and identify the colliding arms.

2) *Static Force Application and Tactile-based Inspection*: Using the external wrench estimate, UAVs are now capable of performing tactile-based tasks such as non-destructive testing, vibration analysis, and leak identification which require a desired wrench to be applied onto a surface in an attempt to reduce safety risks to human workers [24]–[28]. In this context, this work employs *passive* deformable quadrotors to establish smooth contacts and simplify the contact laws [29].

3) *Tactile-based Navigation*: Collision-resilient designs hold a strong potential for a paradigm shift for performing tactile-based navigation [30]–[34]. A motion planner for tactile-based navigation was proposed in [35] consisting of two modes, sliding and flying cartwheel. Authors of [36] utilized vision systems to navigate manhole-sized tubes along with flaps to sense contacts. In [37], collisions were exploited for path planning using sampling-based methods. However, all the works assume prior complete knowledge of the environment.

4) *Mapping*: Conventionally, mapping an environment is performed by using cameras and Structure from Motion (SfM) technique [38] by recreating a 3D structure from a series of images captured from different angles. Research carried out in [39] used the combination of cameras, LiDAR, IMU, and encoders to generate a highly precise map of the environment. Another map generation methodology was presented in [23] where collision detection and localization

TABLE I

Symbol	Definition
$w\mathcal{F} = \{e_1, e_2, e_3\}$	inertial frame
$b\mathcal{F} = \{b_1, b_2, b_3\}$	body fixed frame
$a_i\mathcal{F} = \{a_1^i, a_2^i\}$	$i^{th}$ arm frame with $a_j^i \forall j = 1, 2$ denoting the basis vectors for the $i^{th}$ frame
$x = [x \ y \ z]^T \in \mathbb{R}^3$	3D position of UAV in $w\mathcal{F}$
$v = [\dot{x} \ \dot{y} \ \dot{z}]^T \in \mathbb{R}^3$	3D translational velocity of UAV in $w\mathcal{F}$
$m \in \mathbb{R}, g \in \mathbb{R}$ ,	mass and gravitational acceleration resp.
$R \in \mathbb{R}^{3 \times 3}$	rotation matrix
$\psi \in \mathbb{R}, \dot{\psi} \in \mathbb{R}$	yaw and yawrate respectively
$\hat{\delta}_{f_i} \in \mathbb{R}^3$	estimated force on the $i^{th}$ arm in $w\mathcal{F}$
$\hat{\delta}_{f_{CoM}} \in \mathbb{R}^3$	CoM-based estimated force in $w\mathcal{F}$
$\hat{\delta}_f \in \mathbb{R}^3$	net fused estimated force in $w\mathcal{F}$
$\hat{\delta}_\tau \in \mathbb{R}$	estimated yaw torque in $w\mathcal{F}$
$(\cdot)(\bullet)$	specifies quantity $(\cdot)$ in $(\bullet)$ frame/direction
$\hat{\delta}_f^b \in \mathbb{R}^3 = [\hat{\delta}_f^{b1} \ \hat{\delta}_f^{b2} \ \hat{\delta}_f^{b3}]^T$	denotes $\hat{\delta}_f$ in $b\mathcal{F}$
$C_n \in \mathbb{R}^4$	contact normal to the obstacle
$\lambda \in \{+X, +Y, -X, -Y\}$	move direction of the vehicle
$\Gamma \in \mathbb{R}$	indicates the primitive currently engaged
$d_{step} \in \mathbb{R}$	distance to fly forward in $\Gamma = 1$
$\psi_0 \in \mathbb{R}$	yaw rate threshold to set $\Gamma_{i,i=1,3} \rightarrow \Gamma = 2$
$\delta_0 \in \mathbb{R}$	force threshold to set $\Gamma = 1 \rightarrow \Gamma = 3$
$\delta_{\psi_0} \in \mathbb{R}$	force threshold to set $\Gamma = 2 \rightarrow \Gamma = 3$
$\delta_{f_{des}} \in \mathbb{R}$	force for controlled sliding in $\Gamma = 3$
$\mathcal{W} \in \mathbb{R}$	yaw rate for controlled turning in $\Gamma = 2$

were used to insert obstacle blocks into the point cloud map. However, autonomous planning for performing these missions in unknown low-visible environments where collisions are inevitable remains a challenge. Moreover, previously studied collision-based mapping [40], [41] are error-prone particularly when mapping curved surfaces, making continuous contact-based mapping a desirable approach, as shown in this paper.

### B. Contributions of Present Work

We introduce a novel set of tactile motion primitives for *deformable quadrotors*, enabling real-time contact-based path adaptation and reducing the need for meticulous planning in unstructured environments. The main contributions are:

- 1) A fast-converging external force estimation algorithm for deformable quadrotors, leveraging proprioceptive morphology and onboard accelerometer data.
- 2) Two novel tactile motion primitives for exploration, *Tactile-traversal*, *Tactile-turning*, that adaptively modify the UAV's references based on real-time contact forces.
- 3) A novel 2D *Ricocheting* primitive enabling efficient braking and minimum-time maneuvers by utilizing collision energy dissipation.

Figure 1 and Supplementary Video (Part1) showcase our compliant and passive deformable quadrotor, XPLORER, engaged in various contact-rich tasks. Additionally, Supplementary Material Suppl. includes a literature table detailing the current state-of-the-art from the previous section.

## II. DESIGN AND LOW-LEVEL CONTROL OF XPLORER

In this work, we extend our previous work [12] to develop the deformable quadrotor, XPLORER. Based on a similar concept, XPLORER (Fig. 1) features four deformable arms as part of its morphing chassis, with all four motors aligned in a single plane. This design was chosen for two key reasons. First, it

lowers the center of mass (CoM) compared to our previous design (where the arms were in different planes), reducing the risk of toppling upon contact by shortening the lever arm length during impact. Second, the redesigned propeller guards prevent the UAV from getting stuck in corner cases during exploration, allowing up to  $30^\circ$  of free rotation. Additionally, the current version uses stiffer springs, limiting collision-induced deformation to less than  $30^\circ$ . This enables the UAV to exert forces of approximately 1N on the environment without significant pitching, unlike rigid UAVs, which experience at least  $5^\circ$  of pitch under similar conditions (e.g., a 1.3kg UAV with a thrust-to-weight ratio of 2.82).

The complete control block diagram is shown in Fig. 2 with the notations defined in Table I. The dynamics and other symbols adhere to literature and are described in Suppl. A with the terms  $\delta_f \in \mathbb{R}^3$  and  $\delta_\tau \in \mathbb{R}^3$  denoting the lumped external forces and torques respectively applied on the system and  $f \in \mathbb{R}, \tau \in \mathbb{R}^3$  being the control thrust and torques respectively. The low-level tracking controller is a cascaded P-PID controller that regulates position and attitude errors. Our previous work has successfully demonstrated the robustness of this structure to small inertia errors (arising from short-term ( $\approx 10^\circ$ ) arm angle deviations upon collisions) when paired with a deformable chassis [14], [15]. Hence, we continue to leverage this framework for precise tracking.

## III. EXTERNAL FORCE ESTIMATION AND REACTION

To aid in demonstrating the advantages of deformable chassis, the force estimator should: (1) preserve peak forces upon contact and (2) settle quickly after impact. Towards this, we present the novel force estimator that fuses the proprioceptive state and accelerometer data for faster convergence to true force and isolate the collision location.

### A. Proposed External Force Estimation Algorithm

1) *Force estimate by the spring action at arm:* There are four reference frames  $a_i\mathcal{F}, i = 1..4$ , for each arm as shown in Fig. 3. Now, considering the  $i^{th}$  arm and frame, torque estimate  $\delta_{\tau_i}^{a_i} \in \mathbb{R}$  can be computed by directly using the angular acceleration and rearranging the arm dynamics equation:

$$\mathcal{J}_{zz}\ddot{\theta}_i + b\dot{\theta}_i + k\theta_i = \delta_{\tau_i}^{a_i}, \quad \delta_{\tau_i}^{a_i} = \delta_{f_i}^{a_i}l \quad (1)$$

Here  $\mathcal{J}_{zz}$  is the inertia of the arm about the rotation axis,  $b$  and  $k$  are the damper and spring coefficients respectively and  $\theta_i$  is the deflection in the angle for the  $i^{th}$  arm. The corresponding external force can be computed from  $\delta_{\tau_i}^{a_i} = \delta_{f_i}^{a_i}l$  by assuming that the point of application is at the motor center (which is approximately the arm CoM using SolidWorks estimate), at a constant distance  $l$  from the spring mounting location as shown by Fig. 3. Finally, a first-order low-pass filter is applied, since acceleration can be noisy, to estimate  $\hat{\delta}_{f_i}^{a_i} \in \mathbb{R}^2$ , in arm frame:

$$\hat{\delta}_{f_i}^{a_i} = [K_I(\delta_{f_i}^{a_i} - \hat{\delta}_{f_i}^{a_i}) \ 0]^T \quad (2)$$

where each element corresponds to the components in the direction of the  $i^{th}$  arm's basis and  $K_I$  denotes the filter gain. Now the external force on the  $i^{th}$  arm in the inertial frame,  $\hat{\delta}_{f_i} \in \mathbb{R}^3$ , can be computed by appropriate rotation (Suppl. B)

$$\hat{\delta}_{f_i} = [{}_{a_i}^w R (\hat{\delta}_{f_i}^{a_i}) \ 0]^T \quad (3)$$

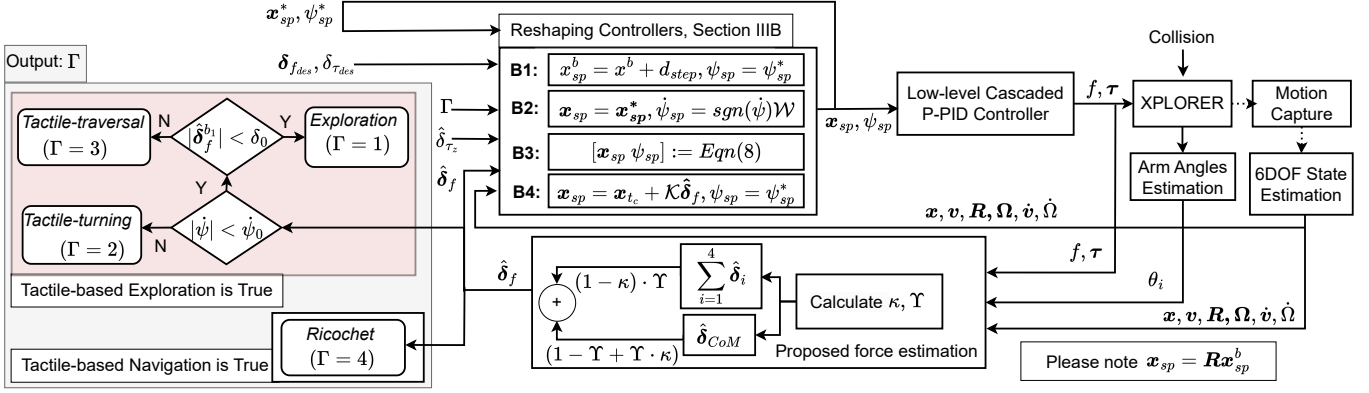


Fig. 2. Block diagram for autonomous tactile exploration and navigation with XPLORER. The external contacts/collisions, characterized in the proposed force estimation block, decide the state of exploration ( $\Gamma$ ) as shown by the flow-chart example (in red). Four reference reshaping controllers are then synthesized to execute the selected  $\Gamma$ , requiring additional inputs of the current reference,  $[\mathbf{x}_{sp}^* \ \psi_{sp}^*]^T$ , current wrench  $[\hat{\delta}_f \ \hat{\delta}_{\tau_z}]^T$  and desired wrench  $[\delta_{f_{des}} \ \delta_{\tau_{des}}]^T$ .

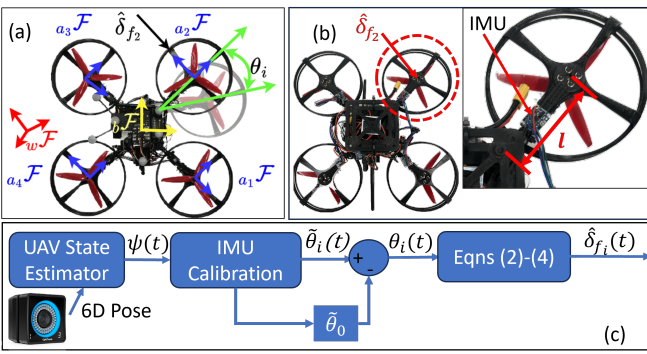


Fig. 3. (a) Frames used to estimate the external force on  $i^{th}$  arm,  $\hat{\delta}_{f_i}$  (b) A zoomed-in view to show the placement of IMU and the assumed point of application of  $\hat{\delta}_{f_i}$  (c) Block diagram for force estimation by spring action.

with  ${}^{w}_{a_i}\mathbf{R}$  being the rotation from  $a_i\mathcal{F}$  frame to  $w\mathcal{F}$  frame.

2) *Force estimate from accelerometer at CoM*: Next, following [23], force information can also be directly estimated using the vehicle's acceleration measurements from the inertial measurement unit (IMU) onboard the flight controller. Upon rearranging the translational dynamics of the UAV and using a median low-pass filter, we get the CoM-based estimate as:

$$\hat{\delta}_{f_{CoM}} = m\dot{v} - mge_3 + f\mathbf{R}e_3 \quad (4)$$

3) *Net estimated force on XPLORER*: The external force obtained from the IMU at CoM has a slower convergence rate than the arm-based estimate. Furthermore, if there is no arm deflection from the external force (e.g. when the force is directly applied at CoM), the estimate based on only arm angle feedback does not converge to the true force, while the estimate from the CoM is correct in this case. In order to make the best use of the two resources and obtain a reliable force estimate, we combine the estimates from both methods. First, define an indicator function to detect contact on the arms

$$\Upsilon = \begin{cases} 1, & \text{if } \sum_{i=1}^4 |\theta_i| > \theta_{th} \\ 0, & \text{otherwise} \end{cases} \quad (5)$$

where  $\theta_i$  is the deflection angle of each arm, and  $\theta_{th}$  is the deflection threshold to detect contact, accounting for backlash. Next, our method for  $\hat{\delta}_f$  fuses  $\hat{\delta}_{f_i}$  3 and (4) to give a fast and accurate estimate with collision arm isolation:

$$\hat{\delta}_f = (1 - \Upsilon + \Upsilon \cdot \kappa) \cdot \hat{\delta}_{f_{CoM}} + (1 - \kappa) \cdot \Upsilon \cdot \sum_{i=1}^4 \hat{\delta}_{f_i} \quad (6)$$

Here  $\kappa \in \mathbb{R}^3 = \xi \hat{\delta}_{f_{CoM}}^{|\cdot|} \triangleq h(\hat{\delta}_{f_{CoM}})$  is an adaptive gain with the tuning parameter  $\xi$ .  $(\cdot)^{|\cdot|}$  denotes the element-wise absolute value of the vector  $(\cdot)$ . Based on (5) and (6), one gives higher weightage to  $\hat{\delta}_{f_{CoM}}$  during collision since the rate of change for  $\hat{\delta}_{f_{CoM}}$  is higher at the collision instant, so  $\kappa$  is larger and the CoM-based estimate is followed. On the other hand, when the wrench estimate from the CoM converges slowly, the rate of change is near zero making the term  $(1 - \kappa)$  is larger, so the total wrench converges to the arm-based estimate. The boundedness and convergence properties of the estimator in (6), and characteristics of  $h$  are discussed in Suppl. C. Additional details for (1) are in Suppl. D and E. Finally, a momentum-based torque observer [23] is implemented to estimate the external torque  $\hat{\delta}_\tau \in \mathbb{R}^3$ . However, only the estimated yaw torque,  $\hat{\delta}_\tau^{e3} \in \mathbb{R}$ , is utilized in tactile-based exploration of the following sections.

## B. Reaction Modes and Controllers for Reference Reshaping

We now introduce the various reference-generation controllers, which reshape the position, yaw, or both references based on external wrench information, enabling different reaction modes.

For all the subsections that follow,  $\mathbf{x}_{sp}^* \in \mathbb{R}^3$  and  $\psi_{sp}^* \in \mathbb{R}$  are the previous reference values of position and yaw respectively in  $w\mathcal{F}$  which are reshaped into  $\mathbf{x}_{sp} \in \mathbb{R}^3$  and  $\psi_{sp} \in \mathbb{R}$  as the final reference position and yaw, in  $w\mathcal{F}$ , for the low-level controller to follow. The complete control block diagram with the interaction controller for XPLORER is shown in Fig. 2.

1) *Free-flight with position disturbance rejection*: In this state, at each instant, the position reference in the body frame for any one direction in  $x-y-z$  is generated using the current value. For example, if we need to only fly forward in  $b\mathcal{F}$ , only  $x^b$  will be reshaped, i.e.  $x_{sp}^b = x^b + d_{step}$  without  $y-z$  or yaw setpoint update. This mode is employed for free-flight exploration and tactile-traversal in Section IV-A.

2) *Continuous yawing*: The UAV remains at its current position ( $\mathbf{x}_{sp} = \mathbf{x}$ ) and continuously turns at a pre-specified constant yaw rate, i.e.  $\dot{\psi}_{sp} = \text{sgn}(\psi)\mathcal{W}$  where  $\mathcal{W}$  is a user-defined constant,  $\text{sgn}$  denotes the sign function.

3) *Static-wrench application*: The reference is reshaped to exert a specific wrench on an object and navigate around it

as described in Section IV-A. A position admittance control strategy is employed towards this by modeling the desired response as a virtual second-order dynamics [12], [23]:

$$\begin{bmatrix} m_v \mathbf{I}_{3 \times 3} & \mathbf{0}_{3 \times 1} \\ \mathbf{0}_{1 \times 3} & \mathcal{I}_{v,z} \end{bmatrix} \begin{bmatrix} \ddot{\mathbf{x}}_{sp} \\ \ddot{\psi}_{sp} \end{bmatrix} + \mathbf{D} \begin{bmatrix} \dot{\mathbf{x}}_{sp} \\ \dot{\psi}_{sp} \end{bmatrix} + \mathbf{K} \begin{bmatrix} \mathbf{x}_{sp} - \mathbf{x}_{sp}^* \\ \psi_{sp} - \psi_{sp}^* \end{bmatrix} = \begin{bmatrix} \hat{\delta}_f - \delta_{f_{des}} \\ \hat{\delta}_\tau^e - \delta_{\tau_{des}} \end{bmatrix} \quad (7)$$

where  $\mathbf{x}_{sp}^*$  and  $\psi_{sp}^*$  are reshaped into  $\mathbf{x}_{sp}$  and  $\psi_{sp}$  respectively by using the external wrench and yaw-torque information -  $\hat{\delta}_f$  and  $\hat{\delta}_\tau^e$ . The virtual parameters employed to reshape the trajectory are the virtual mass,  $m_v \in \mathbb{R}^+$ , inertia about  $z$ ,  $\mathcal{I}_{v,z} \in \mathbb{R}^+$ , and the virtual damping and spring gain matrices,  $\mathbf{D} > 0 \in \mathbb{R}^{4 \times 4}$  and  $\mathbf{K} > 0 \in \mathbb{R}^{4 \times 4}$ .

4) *Collision recovery*: The reference is generated by utilizing the current location and instantaneous collision force. Specifically,  $\mathbf{x}_{sp} = \mathbf{x}_{t_c} + \mathcal{K} \hat{\delta}_f$  with a user defined constant  $\mathcal{K}$  and  $t_c$  denotes the collision instant. The yaw setpoint is not modified. We employ this reaction mode to execute novel *Ricocheting* maneuvers as will be described in Section IV-B.

#### IV. TACTILE-BASED MOTION PRIMITIVES AND MISSIONS

In this section, we present four primitives ( $\Gamma \in \{1, 2, 3, 4\}$ ), for tactile-based exploratory and navigation missions by deformable UAVs. Unlike conventional motion primitives that rely on visual or inertial sensing, our tactile primitives enable navigation purely through contact interactions, making them highly effective in low-visibility or GPS-denied settings. We now state the contact dependent trigger conditions under which a primitive is autonomously engaged and the corresponding controllers from Section III-B that become active.

##### A. Case 1: Tactile-based Exploration and Mapping

1) *Tactile-based Exploration*: The exploration strategy is inspired by the coverage planning algorithms that combine random walk and wall tracing [42]. We introduce this scheme to aerial robots for the first time, demonstrating its effectiveness for deformable UAVs where compliance enables firm and stable contact, offering advantages over rigid UAVs.

The tactile-exploration scheme involves flying forward until encountering an object, then maintaining contact to slide along its surface and turning around its edges to follow its contours. Towards this goal, we define two online decision variables:

- The contact direction,  $\mathbf{C}_n \in \mathbb{R}^4$ : A four-element vector specifying the contact-normal of an object in  $\{\mathbf{b}_1, -\mathbf{b}_1, \mathbf{b}_2$  or  $-\mathbf{b}_2\}$  directions, with  $\|\mathbf{C}_n\|_1 = 1$ . For instance, if  $|\hat{\delta}_f^{b_1}| > \delta_0$  and  $\hat{\delta}_f^{b_1} < 0$ ,  $\mathbf{C}_n = [0 \ 1 \ 0 \ 0]$ , indicating an obstacle along  $\{\mathbf{b}_1\}$  and the contact-normal along  $\{-\mathbf{b}_1\}$ .
- The movement direction,  $\lambda$ : Selects movement direction from the set of  $\{+X, +Y, -X$  or  $-Y\}$ , which corresponds to the  $\{\mathbf{b}_1, \mathbf{b}_2, -\mathbf{b}_1, -\mathbf{b}_2\}$  directions as defined in Table I.

We now present the novel tactile-primitives for exploration (pseudo code in Suppl. F, Algorithms 1-3).

**Exploration**: Initially,  $\Gamma = 1$ , corresponding to free-flight exploration (referred hereon as simply *Exploration*) during which XPLOER experiences negligible yaw torques and external forces. The controller from Section III-B1 is utilized to generate the reference. We set  $d_{step}$  to fly ‘‘forward’’ in the body frame, i.e  $\lambda = +X$ . The trigger condition for entering  $\Gamma = 1$  at any time, is  $(|\dot{\psi}| < \dot{\psi}_0)$  and  $(|\hat{\delta}_f^{b_1}| \text{ or } (|\hat{\delta}_f^{b_2}|)) < \delta_0$ .

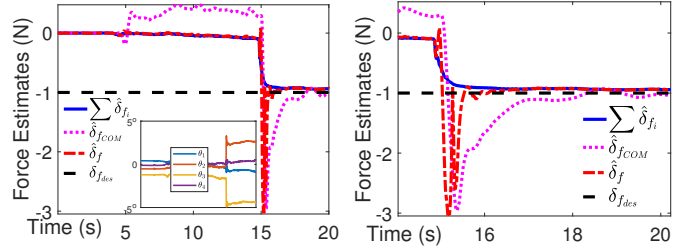


Fig. 4. Results for the proposed force estimation algorithm. Left: Shows estimates for  $\hat{\delta}_f$ ,  $\hat{\delta}_{COM}$  and  $\sum \hat{\delta}_{f_i}$ ; inset shows the corresponding deviation in arm angles. Right: zoomed-in view of the peak.

**Tactile-turning**: The intuition is that upon encountering obstacles’ external edges, the UAV should adjust its yaw to smoothly traverse outward corners allowing for continuous exploration. Towards this, the yaw rate,  $\dot{\psi}$ , is used to detect a high turn rate around a point. This can occur when the vehicle slides along an object’s edge under a desired force, and then releases contact at a corner, causing a sudden spike in  $\dot{\psi}$ . Thus, if  $|\dot{\psi}| > \dot{\psi}_0$ , where  $\dot{\psi}_0$  is the threshold, we set  $\Gamma = 2$  and activate the continuous yawing controller from Section III-B2, allowing the vehicle to rotate around a corner point while monitoring  $\hat{\delta}_f^{b_1}$  (the force in  $\{\mathbf{b}_1\}$  direction). If  $\hat{\delta}_f^{b_1} > \delta_{\psi_0}$  at any time, indicating that further turning is not feasible, we transition to the next exploration state. The threshold  $\dot{\psi}_0$  is chosen adequately to avoid false triggers and  $\psi_{sp}$  is bounded to  $[-\pi \ \pi]$  to avoid yawing indefinitely.

**Tactile-traversal**: The intuition is that if the UAV encounters an object while flying forward, it should slide along its contour to adapt its path. Additionally, applying a controlled force while sliding will ensure stable contact for continuous wall-following and enable shape reconstruction. The sudden force release at edges or gaps will induce a high turn rate and autonomously trigger tactile-turning for rapid reorientation. Accordingly, the forward contact force is monitored such that if  $|\hat{\delta}_f^{b_1}|$  or  $|\hat{\delta}_f^{b_2}| > \delta_0$ , the vehicle is experiencing immovable force, setting  $\Gamma = 3$ . The *Tactile-traversal* primitive utilizes controllers from Sections III-B1 and III-B3 for controlled sliding. We set  $\lambda$  orthogonal to  $\mathbf{C}_n$  following a right-side rule.

For instance, if  $\mathbf{C}_n = [0 \ 1 \ 0 \ 0]$ ,  $\lambda = +Y$  and the next waypoint is first generated utilizing the controller in Section III-B1 with  $d_{step}$  for motion in  $+Y$ . The interaction controller from Section III-B3 then reshapes it to ensure that the vehicle maintains contact with the obstacle by exerting a desired force on it while sliding across it, as shown in Fig. 1(ii). Specifically,  $\delta_{f_{des}} = [\Delta_{f_{des}} \ 0 \ 0]^T$  and  $\delta_{\tau_{des}} = \hat{\delta}_\tau^{e3}$  to enable force exertion in  $+X$ , flying in  $+Y$  and yielding to any yaw torques.

*Remark 1*:  $\delta_{\psi_0}$  is chosen slightly higher than  $\delta_0$  to ensure fail-safe behavior while transitioning from  $\Gamma = 2$  to  $\Gamma = 3$ .

2) *Tactile-based Mapping*: The ability to explore the environment while maintaining contact can be utilized to generate an obstacle map. This map can then be used for motion planning by XPLOER or other autonomous robots. The algorithm utilizes the  $\hat{\delta}_f$ , the CAD model of XPLOER, and the global pose to generate the obstacle boundary map. We use the Open3D library [43] to process the point cloud generated.

Obstacle map generation initializes if the estimated force is above the threshold, i.e.,  $|\hat{\delta}_f^{b_1}|$  or  $|\hat{\delta}_f^{b_2}| \geq \delta_{map}$  and if the UAV is flying.  $\delta_{map}$  is taken to be slightly higher than  $f_{des}$  to

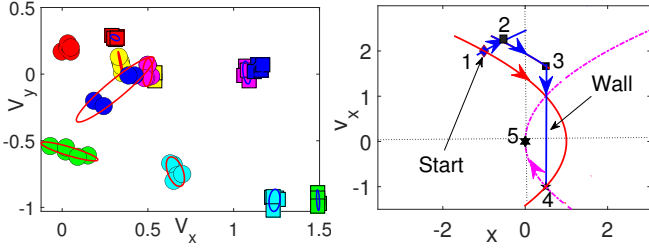


Fig. 5. Left: Collision experiments to understand ricocheting. Symbols  $\square$  and the  $\circ$  represent the pre and post-collision velocities of each case (distinguished by color). Right: Simulation phase-portrait to demonstrate ricocheting (path 1-2-3-4-5) vs conventional (path 1-4-5). The curves represent constant acceleration for a second order system,  $\ddot{x} = u$ , with  $u$  as the input.

ensure mapping is conducted only when there is firm contact with the obstacle. A rigid object of dimension  $0.25 \text{ m} \times 0.08 \text{ m} \times 0.5 \text{ m}$  is added to the point cloud at a small offset from the CoM of XPLOER in the direction of  $C_n$ , which provides the outward normal of the obstacle for shape reconstruction.

To handle internal corners, we utilize the previous and current move directions to determine object placement. Specifically, when the move direction,  $\lambda$  differs from the previous one, it typically indicates a corner, prompting the addition of a fixed point cloud diagonally with a  $0.417 \text{ m}$  offset to ensure map continuity. These parameters were selected to suit indoor environments and improve mapping accuracy.

The point cloud map is generated at a frequency of  $30 \text{ Hz}$  to achieve a high-resolution representation of the obstacle. It is stored in Polygon File Format (PLY) in ASCII format, containing the coordinates of each point in the cloud. The map generation process was carried out on a computer equipped with an AMD Ryzen 5 CPU and  $16 \text{ GB}$  of RAM. The position and wrench estimates are recorded on the ground computer and relayed from the high-level companion computer via ROS2 network. An overview of the framework is in Suppl. Alg. 4.

### B. Case 2: Tactile-based Navigation - Ricocheting

We now introduce *Ricocheting* – a tactile-based primitive for fast braking by bouncing-off objects.

First, we collected experimental data for six different collision velocities with two different heading angles (at  $\psi = 90^\circ$ ,  $45^\circ$ ) with five trials each, totaling  $60$  flights to understand the post-collision dynamics. In all the experiments, the recovery controller from Section III-B4 is employed to generate the post collision waypoint. The scatter plots for these experiments are shown in Fig. 5, along with the error ellipses. We noticed that the heading angle didn’t influence the post collision state significantly. Moreover, in all the experiments, there was energy loss due to the damping introduced by the deformable chassis resulting in dissipation of energy which combined with the recovery controller, facilitates a fast stopping maneuver.

This enables us to define *Ricocheting* ( $\Gamma = 4$ ), as a maneuver where collisions between the UAV and environment serve as jump maps to facilitate minimum-time trajectories. Following the time-optimal control approach for hybrid double integrators with state-driven jumps in [44], simulation results in Fig. 5(b) show that the path 1-2-3-4-5 is shorter than 1-4-5 when state jumps are allowed (the complete derivation is in Suppl. G). However, the UAV ricocheting problem differs

from the setting in [44] because “collisions” serve as jump maps, which cannot be activated arbitrarily at any location. Therefore, we developed a neural network (CollisionNet) to analyze the rebound velocities for the data collected (details in Suppl. H) and propose the condition whether or not to ricochet.

*When to Ricochet:* If a collision node lies within a circle of radius  $\zeta$  of the stopping node (marked in Fig. 1(a3)), ricochet off that node at maximum velocity attainable to reach the stopping node in minimum time. The post-collision velocities can be verified online via the CollisionNet developed before engaging  $\Gamma = 4$ . We choose  $\zeta = 0.5 \text{ m}$ .

*Remark 2:* In most experiments, collisions introduced an undesired downward force, so we avoid exploiting momentum changes along  $e_3$  and focus only on in-plane (2D) collisions (hence a circle in the above condition). Moreover, as heading angle changes have a minor impact on momentum relative to the pre-collision velocity, any 2D maneuver can be effectively reduced to 1D for multirotors, ensuring the condition is valid.

*Remark 3:* Significant variation in the post collision state at higher velocities (large blue and green scatter groups in Fig. 5) warrant thorough collision modeling to better understand impact dynamics. Such modeling is essential for proposing new maneuvers at higher velocities, beyond those introduced in this article.

## V. EXPERIMENTAL RESULTS AND DISCUSSION

### A. Experimental Setup, Sensors and Control Parameters

1) *Experimental Setup:* The low-level controller utilized is a PIXHAWK flight controller with the RaspberryPi4B as the companion computer. The companion computer relays the position and orientation of the vehicle from an indoor motion capture system to the flight controller at  $120 \text{ Hz}$ . A  $4 \text{ S}$  lithium polymer battery of  $3300 \text{ mAh}$  LiPo battery of  $14.8 \text{ V}$ ,  $50 \text{ C}$  is used for the power supply. The motors are controlled utilizing Lumenier 30A BLHeli\_S Electronic Speed Controllers and the entire system has a mass of  $1.12 \text{ kg}$ . Our experimental testbed consists of four distinct environments that closely resemble real-world flight spaces and help in validating the tactile-based exploration and navigation algorithms. (i) a rectangular object measuring  $1.22 \text{ m} \times 1.0 \text{ m}$  was set up using acrylic panels (ii) acrylic panels were organized to represent a box with XPLOER’s initial state outside the box (iii) a trash can and (iv) a vertical pipe to represent real obstacles.

2) *Sensors for Arm-based Force Estimates:* We employ four low-cost off-the-shelf 9-DOF IMUs (BNO055, Adafruit, New York, NY) on XPLOER (one on each arm) to get the angular acceleration and estimate the external force on the arm. They are connected to the companion computer via serial communication at  $50 \text{ Hz}$ . The Euler angles are computed using the Adafruit BNO055 library. A median low-pass with a band-stop filter is employed to obtain accurate estimates of the arm angles,  $\theta_i$ , at any given instant. This is used to estimate the arm wrench  $\hat{\delta}_{f_i}$  in Section III-A1.

3) *Thrust Estimate and Interaction Controller Parameters:* In order to calculate the wrench at the CoM, the controller’s normalized force and torque values are obtained from the on-board flight controller. The force value is obtained empirically

TABLE II  
PARAMETERS & THRESHOLDS USED IN EXPERIMENTS

Parameter	Threshold Value	Parameter	Threshold Value
$\psi_0$	0.4 rad/s	$d_{step}$	0.25 m
$\mathcal{W}$	0.26 rad/s	$\Delta_{f_{des}}$	1.25 N
$\delta_0$	1.5 N	$\delta_{map}$	1.51 N
$\delta_{\psi_0}$	1.6 N	$\mathcal{K}$	0.1

and used to calculate the approximate value of the actual thrust. This technique can be improved by performing a PWM-thrust mapping curve using RPM sensor feedback. Gains for the interaction controller in (7) are tuned by experiments to be:  $\mathbf{D} = \mathbf{K} = \text{diag}(24.5, 24.5, 0, 1)$ ,  $m_v = \mathcal{I}_{v,z} = 1$ .

### B. Force Estimation Algorithm Validation

A static wrench application task is performed to validate the force estimation algorithm as shown in Fig. 4. The reference for this experiment is set to  $\delta_{f_{des}} = [-1 \ 0 \ 0]^T$  for applying a 1 N force on the wall. We use a load cell (ATO Micro 5kg Tension and Compression Load Cell, S Type, ATO, Diamond Bar, CA) with a sampling rate of 20Hz, mounted on the wall, to obtain the ground truth. A digital reader is attached to the load cell which is calibrated to display the force readings when the load cell is compressed. The UAV takes off and starts applying force on the box whose other end pushes the load cell. Wrench validation experiments are shown in Supplementary Video, SVideo (Part2).

The inset plot in Fig. 4, shows the deviation of the arm angles upon contact. The estimate from the CoM (magenta dotted line) takes time to converge, however, the arm-based force estimate (blue solid) converges sooner without the collision peak. By fusing both methods, the proposed estimate (red dashed) retains the peak from the CoM-based method and also converges faster. For this experiment, the true force applied on the wall was collected and averaged over 2s after impact, to be approximately 1.31N, demonstrating an accuracy of  $\approx 77\%$ . We also conduct experiments where there is no contact to show  $\hat{\delta}_{f} = \hat{\delta}_{f_{CoM}}$  (SVideo Part2, Suppl. E, pulley experiment).

### C. Autonomous Tactile-based Exploration and Mapping

In this section, we present the experimental results for the exploration and mapping mission applied to map a wall, a box, an acrylic pipe, and a trashcan as shown in Figs. 6 and 7.

The mission begins with XPLORER taking off to a hover height of 0.7m and initiating the *Exploration* state ( $\Gamma = 1$ ), moving forward until an obstacle is detected. It then pushes against the surface until the threshold for *Tactile-traversal* is reached, triggering a transition to *Tactile-traversal* ( $\Gamma = 3$ ), where it slides along the obstacle's surface. This  $1 \rightarrow 3$  transition is illustrated in Fig. 6i.

If the vehicle encounters an outward corner (e.g., on a box) that induces a sudden yaw, it transitions to *Tactile-turning* ( $\Gamma = 2$ ) to perform a controlled turn and establish contact with the next surface, before returning to *Tactile-traversal* ( $\Gamma = 3$ ). For box-like structures, the full state sequence becomes  $1 \rightarrow 3 \rightarrow 2 \rightarrow 3$ , as shown in 7.

*Remark 4:* Performance of the exploratory algorithm relies on threshold values which are influenced by friction and aerodynamic wrenches acting on XPLORER. Through extensive testing, we identified threshold values that perform reliably

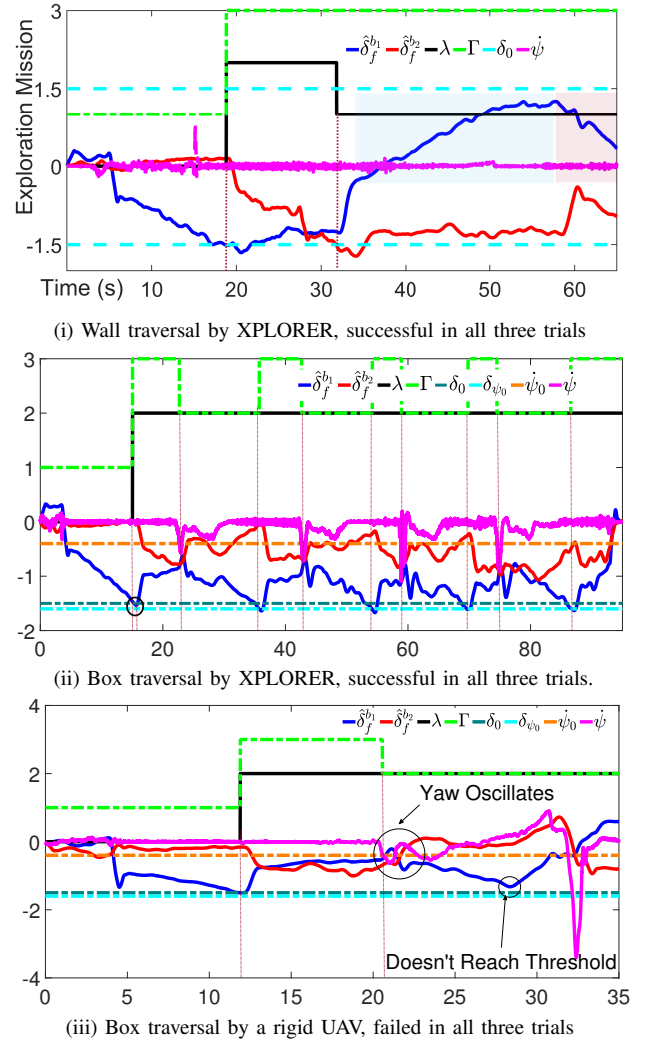


Fig. 6. Experimental results for tactile-based exploration. (i) XPLORER navigating a wall-like structure, activating  $\Gamma = 1,3$  when  $\delta_0$  is crossed. Blue and red regions indicate unmodeled frictional and wall effects. (ii) XPLORER navigating a box-like structure, activating  $\Gamma = 1,2,3$  when  $\delta_0$  or  $\psi_0$  are crossed. (iii) A rigid UAV fails to engage *Tactile-traversal* after *Tactile-turning* due to chassis rigidity, resulting in oscillatory yaw motion at convex corners.

in indoor environments, as shown in Table II. While the compliant chassis allows these parameters to generalize across a broad range, accurately updating the desired interaction wrench remains challenging and is an active area of research.

*Note:* The state machine applies a moving average filter (50 samples) on  $\hat{\delta}_f$ , and a low-pass filter on  $\psi$  to mitigate noise effects during decision-making.

1) *Wall-traversal:* In this experiment, XPLORER navigates across a wall edge.  $\Gamma$  switches between 1 and 3 only as shown by the green line in Fig. 6i and SVideo (Part3a); the yaw-rate never crosses  $\psi_0$  for *Tactile-turning* to be engaged. The mapping algorithm follows the description in Section IV-A2 and the generated map is shown in the inset of Fig. 7.

2) *Box-traversal:* In this experiment, XPLORER navigates around a box. From Fig. 6ii,  $\Gamma$  correctly switches between values of 1, 2, and 3 whilst circumnavigating the obstacle. The box dimensions extracted from the generated map (inset of Fig. 7) are  $1.231\text{m} \times 1.019\text{m}$ , compared to the actual dimensions of  $1.22\text{m} \times 1.0\text{m}$ , yielding an area estimation accuracy of  $\approx 96.72\%$ . The results are demonstrated in SVideo (Part 3b).

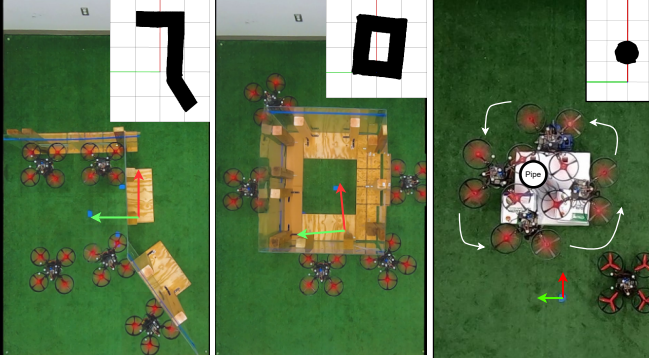


Fig. 7. Top view of the mapping experiments with the corresponding maps generated, in the insets for a box, a wall and an acrylic pipe.

3) *Pipe outer diameter traversal*: This test case demonstrates the tactile-based exploration algorithm’s capability to navigate circular objects. The generated map in the inset of Fig. 7 and SVideo (Part3c) for this particular scenario, is within 86% of the actual dimensions of the pipe. Compared to the previous scenario, the drop in mapping accuracy is possibly due to instances when XPLOER momentarily loses contact with the pipe before re-establishing contact.

4) *Trash can traversal*: This case presents a partial success scenario when during tactile-based exploration, XPLOER loses contact (final edge of the trash can in SVideo (Part3c)). The combination of a low-friction surface, the can’s size relative to XPLOER’s width, and insufficiently tuned virtual parameters in (7) likely results in inadequate  $\psi$  at the corner, preventing the system from transitioning into the *Tactile-turning* state. The mission is manually terminated here. In the future, design modifications and online tuning of controller parameters can be looked into to prevent such failures.

5) *Comparison against a Rigid UAV*: We conducted both wall-traversal and box-traversal experiments for a similar dimension rigid UAV and only the wall-traversal exploration with inward edges was successful. For a box-like obstacle, the rigid UAV initially is successful in engaging  $\Gamma$  as  $1 \rightarrow 3 \rightarrow 2$  systematically as shown by the green line in Fig. 6iii. However, after the turning maneuver in  $\Gamma = 2$ , significant oscillations are observed in yaw and the UAV was not able to maintain consistent contact, possibly due to absence of compliance and damping in the chassis. Consequently,  $\Gamma = 3$  was never engaged as compared to the XPLOER case, where reengagement happened around 37s as shown in Fig. 6ii. Similar behaviors are observed in all four experiments conducted for this case, and the exploration scheme for a rigid drone failed. Experimental videos are presented in SVideo (Part3d).

*Note*: Additional validation results are presented in SVideo Part3c for objects with slots. It is also observed that in some cases when the rigid UAV makes contact in *Exploration* state, significant yaw torque disturbance (due to the large impacts) falsely triggered the *Tactile-turning* state, reinforcing that the proposed tactile-based exploration scheme is suitable for deformable UAVs. These results are presented in Suppl. I.

#### D. Waypoint Tracking via Ricocheting

In this subsection, we present the benefits of ricocheting via two cases. In the first case, the goal ( $[0.3 \ 0 \ -0.75]^T$  m) is

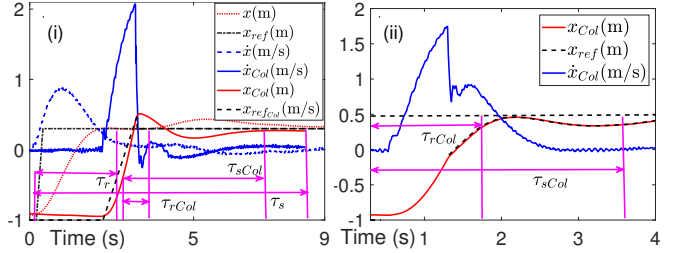


Fig. 8. Trajectories of three ricocheting experiments. (i) Goal is near the wall, shows both with- and without- ricocheting. (ii) Goal location is beyond wall, ricocheting off the edge. In all cases, ricocheting maneuvers are time-optimal.

near the wall ( $x_{wall} = 0.5$  m) to facilitate *ricocheting off the wall’s face* with a velocity of  $[\dot{x}^-, \dot{y}^-]^T = [2, 0]^T$  m/s. In the second case, the goal ( $[0.5 \ 0 \ -0.75]^T$  m) is set some distance beyond the wall ( $x_{wall} = 0$  m) to enable *ricocheting off the edge* with  $[\dot{x}^-, \dot{y}^-]^T = [1.75, 0]^T$  m/s. For both the cases, the start location is  $[-1 \ 0 \ -0.75]^T$  m. The pre-collision velocities were the maximum velocities that could be attained in the closed space and are verified by the CollisionNet in Section. IV-B to have reduced rebound velocities upon impact. The rise time ( $\tau_r$ ) and settling time ( $\tau_s$ ) are chosen as the metrics to evaluate the performance of ricocheting.

For the first case scenario with the goal near the wall, the conventional, collision-exclusive trajectory is shown in Fig. 8i, where the vehicle first accelerates, then decelerates to reach the setpoint. There is an overshoot which it tries to minimize, slowly converging to the reference. The  $\tau_r$  and  $\tau_s$  are noted to be 2.27 and 8.995 seconds, respectively. Furthermore, over three trials the RMSE error was around  $\pm 3$  cm for this case. In contrast, the experimental results for ricocheting show that XPLOER reaches the wall with maximum velocity, collides, and stops at the wall almost instantaneously by dissipating kinetic energies as shown by the plots in Fig. 8i. The  $\tau_{rCol}$  (subscript  $Col$  denotes experiments with collision) and  $\tau_{sCol}$  are calculated to be 1.046 and 5.292 seconds, respectively which are faster than the conventional trajectories. Over six trials, the RMSE error was  $\pm 0.5$  cm.

For the second case where the vehicle performs ricocheting off the edge and regulates itself to a setpoint beyond the wall, results in Fig. 8ii show significantly shorter flight time with  $\tau_{rCol} = 1.685$  seconds and  $\tau_{sCol} = 3.631$  seconds, respectively. The flight test results are shown in SVideo (Part4).

For both cases, it is seen that *Ricocheting* with the current recovery controller yielded agile maneuvers with shorter flight time by incorporating a collision-based velocity state-jump. This highlights the advantages of collisions for planning novel pursuit/evade maneuvers and agile navigation.

## VI. CONCLUSION

### A. Summary

In this work, we presented an autonomous exploration and navigation framework for deformable UAVs through real-time trajectory modifications. Unlike conventional motion primitives, our tactile primitives adapt dynamically to surface interactions, improving navigation and tactile mapping. Experiments showed that tactile-turning allows UAVs to execute

smooth corner traversal, while tactile-traversal ensures continuous surface contact for reliable wall-following. Additionally, our force estimation algorithm effectively triggered these primitives, enabling robust autonomous decision-making. We also introduced ricocheting, leveraging collision-induced state jumps for minimum-time braking and trajectory redirection.

The proposed tactile-based exploration and navigation methodology demonstrates that deformable UAVs can interact with their environment in ways rigid UAVs cannot, unlocking new capabilities for autonomous navigation, inspection, and surveillance in constrained, contact-rich environments.

## B. Discussion and Future Directions

Future research can focus on developing detailed collision models to enable new maneuvers in 3D space beyond those proposed in this article. These behaviors could be integrated into online motion planning algorithms, such as RRT\*, for improved real-time trajectory adjustments. Another direction is to use learning-based strategies to adapt the virtual stiffness ( $\mathbf{K}$ ) and damping ( $\mathbf{D}$ ) parameters and exploration step size ( $d_{step}$ ) based on surface properties for robust interaction. Incorporating tactile sensing with visual-inertial odometry could strengthen navigation in GPS-denied or low-visibility settings. Finally, advanced Kalman filtering techniques could be explored to fuse proprioceptive data for wrench estimates, improving accuracy for various conditions. Together, these directions could significantly broaden the capabilities of UAVs for physical interaction in complex environments.

## VII. ACKNOWLEDGMENTS

The authors thank YiZhaung Garrard, Bill Nguyen and Yogesh Kumar from the ASU RISE lab for the brainstorming sessions and help with experiments.

## REFERENCES

- [1] F. Ruggiero *et al.*, “Aerial manipulation: A literature review,” *IEEE Robot. Autom. Lett.*, vol. 3, no. 3, pp. 1957–1964, 2018.
- [2] D. Hausmann *et al.*, “Monitoring of gas pipelines—a civil uav application,” *Aircraft Eng. Aero. Tech.*, vol. 77, no. 5, pp. 352–360, 2005.
- [3] S. Mishra *et al.*, “Autonomous vision-guided object collection from water surfaces with a customized multirotor,” *IEEE/ASME Trans. Mech.*, vol. 26, no. 4, pp. 1914–1922, 2021.
- [4] S. Kim *et al.*, “Aerial manipulation using a quadrotor with a 2dof robotic arm,” in *IEEE/RSJ Int. Conf. Intl. Robot. Sys.*, pp. 4990–4995, 2013.
- [5] A. Suarez *et al.*, “Lightweight compliant arm for aerial manipulation,” in *IEEE/RSJ Int. Conf. Intl. Robot. Sys.*, pp. 1627–1632, 2015.
- [6] A. Bredenbeck *et al.*, “Embodying compliant touch on drones for aerial tactile navigation,” *IEEE Robot. Autom. Lett.*, vol. 10, no. 2, pp. 1209–1216, 2024.
- [7] M. Kovac, “Learning from nature how to land aerial robots,” *Science*, vol. 352, no. 6288, pp. 895–896, 2016.
- [8] S. Minchev and D. Floreano, “Adaptive morphology,” *IEEE Robot. Autom. Mag.*, vol. 23, no. 3, pp. 42–54, 2016.
- [9] W. Tao *et al.*, “Design, characterization and control of a whole-body grasping and perching (WHOPPER) drone,” in *IEEE/RSJ Int. Conf. Intl. Robot. Sys.*, pp. 1–7, IEEE, 2023.
- [10] K. Patnaik and W. Zhang, “Adaptive attitude control for foldable quadrotors,” *IEEE Control Systems Letters*, 2023.
- [11] K. Patnaik and W. Zhang, “Towards reconfigurable and flexible multirotors,” *Int. J. Intel. Robot. App.*, vol. 5, no. 3, pp. 365–380, 2021.
- [12] K. Patnaik *et al.*, “Design and control of squeeze,” in *IEEE/RSJ Int. Conf. Intl. Robot. Sys.*, pp. 1364–1370, 2020.
- [13] Z. Liu and K. Karydis, “Toward impact-resilient quadrotor design, collision characterization and recovery control to sustain flight after collisions,” in *IEEE Int. Conf. Robot. Autom.*, pp. 183–189, 2021.
- [14] K. Patnaik *et al.*, “Collision recovery control of a foldable quadrotor,” in *IEEE/ASME Int. Conf. Adv. Intl. Mech.*, pp. 418–423, 2021.
- [15] P. H. Nguyen, K. Patnaik, *et al.*, “A soft-bodied aerial robot for collision resilience and contact-reactive perching,” *Soft Robotics*, 2023.
- [16] V. Serbezov *et al.*, “Application of multi-axis force/torque sensor system,” *IOP Conf. Mater. Sci. and Eng.*, vol. 878, no. 1, p. 012039, 2020.
- [17] A. Ollero *et al.*, “The aeroarms project,” *IEEE Robot. Autom. Mag.*, vol. 25, no. 4, pp. 12–23, 2018.
- [18] F. Ruggiero *et al.*, “Impedance control of vtol uavs with a momentum-based external generalized forces estimator,” in *IEEE Int. Conf. Robot. Autom.*, pp. 2093–2099, 2014.
- [19] F. Ruggiero *et al.*, “Passivity-based control of vtol uavs with a momentum-based estimator of external wrench and unmodeled dynamics,” *Robot. Auto. Sys.*, vol. 72, pp. 139–151, 2015.
- [20] B. Yüksel *et al.*, “A nonlinear force observer for quadrotors and application to physical interactive tasks,” in *IEEE/ASME Int. Conf. Adv. Intl. Mech.*, pp. 433–440, 2014.
- [21] M. Ryll *et al.*, “6d interaction control with aerial robots: The flying end-effector paradigm,” *Int. J. Robot. Research*, vol. 38, no. 9, pp. 1045–1062, 2019.
- [22] C. D. McKinnon and A. P. Schoellig, “Unscented external force and torque estimation for quadrotors,” in *IEEE/RSJ Int. Conf. Intl. Robot. Sys.*, pp. 5651–5657, 2016.
- [23] T. Tomić *et al.*, “External wrench estimation, collision detection, and reflex reaction for flying robots,” *IEEE Trans. Robot.*, vol. 33, no. 6, pp. 1467–1482, 2017.
- [24] P. Pfändler *et al.*, “Flying corrosion inspection robot for corrosion monitoring of civil structures—first results,” in *SMAR Conf. on Smart Moni. Assess. Rehab. Civil Struc. Prog.*, pp. We–4, 2019.
- [25] J. Hu, S. Zhang, E. Chen, and W. Li, “A review on corrosion detection and protection of existing reinforced concrete (rc) structures,” *Construction and Building Materials*, vol. 325, p. 126718, 2022.
- [26] K. Alexis *et al.*, “Aerial robotic contact-based inspection: planning and control,” *Autonomous Robots*, vol. 40, pp. 631–655, 2016.
- [27] K. Bodie *et al.*, “Active interaction force control for contact-based inspection with a fully actuated aerial vehicle,” *IEEE Trans. Robot.*, vol. 37, no. 3, pp. 709–722, 2020.
- [28] M. Tognon *et al.*, “A truly-redundant aerial manipulator system with application to push-and-slide inspection in industrial plants,” *IEEE Robot. Autom. Lett.*, vol. 4, no. 2, pp. 1846–1851, 2019.
- [29] B. Brogliato, *Nonsmooth mechanics*, vol. 3. Springer, 1999.
- [30] J.-C. Zufferey, A. Beyeler, and D. Floreano, “Optic flow to steer and avoid collisions in 3d,” *Flying Insects and Robots*, pp. 73–86, 2010.
- [31] D. Schafroth, S. Bouabdallah, C. Bermes, and R. Siegwart, “From the test benches to the first prototype of the muffy micro helicopter,” *J. Intel. Robot. Sys.*, vol. 54, pp. 245–260, 2009.
- [32] R. He, A. Bachrach, and N. Roy, “Efficient planning under uncertainty for a target-tracking micro-aerial vehicle,” in *IEEE Int. Conf. Robot. Autom.*, pp. 1–8, 2010.
- [33] S. Shen, N. Michael, and V. Kumar, “Autonomous multi-floor indoor navigation with a computationally constrained mav,” in *IEEE Int. Conf. Robot. Autom.*, pp. 20–25, 2011.
- [34] D. Scaramuzza *et al.*, “Vision-controlled micro flying robots,” *IEEE Robot. Autom. Mag.*, vol. 21, no. 3, pp. 26–40, 2014.
- [35] N. Khedekar *et al.*, “Contact-based navigation path planning for aerial robots,” in *Int. Conf. Robot. Autom.*, pp. 4161–4167, IEEE, 2019.
- [36] P. De Petris *et al.*, “Resilient collision-tolerant navigation in confined environments,” in *IEEE Int. Conf. Robot. Autom.*, pp. 2286–2292, 2021.
- [37] J. Zha and M. W. Mueller, “Exploiting collisions for sampling-based multicopter motion planning,” in *IEEE Int. Conf. Robot. Autom.*, pp. 7943–7949, 2021.
- [38] J. L. Schonberger and J.-M. Frahm, “Structure-from-motion revisited,” in *Proc. IEEE Conf. Comput. Vis. Patt. Recog.*, pp. 4104–4113, 2016.
- [39] D. Cattaneo *et al.*, “Cmrnet: Camera to lidar-map registration,” in *IEEE Intel. Transp. Sys. Conf.*, pp. 1283–1289, 2019.
- [40] Y. Mulgaonkar *et al.*, “The tiercel: A novel autonomous micro aerial vehicle that can map the environment by flying into obstacles,” in *Int. Conf. Robot. Automation*, pp. 7448–7454, IEEE, 2020.
- [41] A. Briod *et al.*, “Contact-based navigation for an autonomous flying robot,” in *IEEE/RSJ Int. Conf. Intl. Robot. Sys.*, pp. 3987–3992, 2013.
- [42] K. M. Hasan *et al.*, “Path planning algorithm for autonomous vacuum cleaner robots,” in *Int. Conf. Info. Elec. Vis.*, pp. 1–6, IEEE, 2014.
- [43] Q.-Y. Zhou, J. Park, and V. Koltun, “Open3D: A modern library for 3D data processing,” *arXiv:1801.09847*, 2018.
- [44] A. Cristofaro *et al.*, “Time-optimal control for the hybrid double integrator with state-driven jumps,” in *IEEE Conf. Decision. Control*, pp. 6301–6306, 2019.



TABLE III  
COMPARISON WITH EXISTING LITERATURE FOR UAV-BASED TACTILE APPLICATIONS

Article	Type		Wrench Information	New UAV Primitives	Planning	Mapping Contours	Min. Time Braking
	Chassis	Extra					
Bredenbeck A. et. al [6]	rigid	finger	finger (joint encoders)	end-effector based	online	no	no
Alexis, K. et al [26]	rigid	none	– (planning is independent)	RRT* and LKH for TSP	offboard	no	no
Bodie K. et. al [27]	rigid	arm	force-torque sensors	– (existing vision + tree-lookup)	online	yes	no
Tognon, M. et al [28]	rigid	arm	– (planning is independent)	– (existing control-aware plan)	offboard	yes	no
Khedekar N. et al. [35]	rigid	none	– (assumes known surface)	flying-cartwheel, sliding	offline	no	no
P. De Petris et al. [36]	rigid	flap	flex sensors	adaptive acceleration	online	no	no
Mulgaonkar Y. et al. [40]	rigid	none	onboard IMU sensors	reflected-ray based waypoint	online	2D rectilinear	no
Briod A. et al. [41]	deformable	none	onboard IMU sensors	random exploration based wp	online	only walls	no
<b>XPLORER</b>	<b>deformable</b>	<b>none</b>	<b>arm orientation sensor with onboard IMU</b>	<b>contact-based reactive primitives (tactile turning, traversal, ricocheting)</b>	<b>online</b>	<b>wall, pipe, box, trashcan</b>	<b>yes</b>

TABLE IV  
COMPARISON WITH EXISTING LITERATURE FOR UAV WRENCH ESTIMATION TECHNIQUES

Article	New Method		Sensors Needed	Estimation Technique	Collision Isolation	Application Demonstrated
	Force	Torque				
Ruggiero, F. et al. [19]	yes	yes	onboard IMU sensors	momentum-based	no	low-level control design
Yüksel, B. et al. [20]	yes	yes	–	a Lyapunov based observer	–	– (only simulations)
McKinnon & Schoellig [22]	yes	yes	onboard IMU sensors	UKF based observer	no	admittance control design
Tomić, Teodor [23]	yes	yes	onboard IMU sensors	hybrid-based	yes	collision-recovery
<b>XPLORER</b>	yes	<b>no</b>	<b>onboard IMU, 4 BNO055</b>	<b>acceleration-based, hybrid fusing of CoM and proprioceptive</b>	<b>collision arm identified</b>	<b>tactile-based exploration, mapping and collision recovery</b>

## APPENDIX

### A. Quadrotor Dynamics

Considering the net body thrust,  $f \in \mathbb{R}$ , and the body torques,  $\tau \in \mathbb{R}^3$ , as the control inputs, the rigid-body dynamics can be written as:

$$\begin{aligned} \dot{\mathbf{x}} &= \mathbf{v} \\ m\dot{\mathbf{v}} &= m\mathbf{g}e_3 - f\mathbf{R}e_3 + \delta_f \end{aligned} \quad (8a)$$

$$\begin{aligned} \dot{\mathbf{R}} &= \mathbf{R}\hat{\Omega} \\ \mathbf{H}\dot{\hat{\Omega}} - [\mathbf{H}\hat{\Omega}]_{\times}\hat{\Omega} &= \tau + \delta_{\tau} \end{aligned} \quad (8b)$$

where  $m$ ,  $\mathbf{H}$  denote the mass and inertia of XPLORER respectively, and  $\mathbf{x} \in \mathbb{R}^3$  and  $\mathbf{v} \in \mathbb{R}^3$  denote the 3D position and translational velocity, respectively. The other symbols adhere to literature [12]. The terms  $\delta_f \in \mathbb{R}^3$  and  $\delta_{\tau} \in \mathbb{R}^3$  denote the lumped external forces and torques respectively applied on the system. The *hat map*  $\hat{\cdot} : \mathbb{R}^3 \rightarrow \text{SO}(3)$  is a symmetric matrix operator defined by the condition that  $\hat{\mathbf{x}}\mathbf{y} = \mathbf{x} \times \mathbf{y} \forall \mathbf{x}, \mathbf{y} \in \mathbb{R}^3$  and  $[\cdot]_{\times}$  is the skew symmetric cross product matrix.

### B. Rotation from the Arm Frame to Body Frame

The rotation matrix for converting a vector in the arm frame  ${}_{a_i}\mathcal{F}$ , to body frame  ${}_b\mathcal{F}$ , is given by (9) below

$${}^b_{a_i}\mathbf{R} = \begin{bmatrix} \cos \varphi_i & -\sin \varphi_i & 0 \\ \sin \varphi_i & \cos \varphi_i & 0 \\ 0 & 0 & 1 \end{bmatrix} \quad (9)$$

with  $\varphi_i$  being the arm angle deflection for the  $i^{\text{th}}$  arm calculated as  $\varphi_i = (\nu_i + \mu_i + \theta_i)$  and  $\nu_i = \frac{-\pi}{2}$  for  $i = 1, 2$  and  $\nu_i = \frac{+\pi}{2}$  for  $i = 3, 4$  and  $\mu_i = \{\frac{3\pi}{4}, \frac{\pi}{4}, \frac{-\pi}{4}, \frac{-3\pi}{4}\}$  for  $i = \{1, 2, 3, 4\}$  respectively. Along with (3), this gives the force estimate from spring action in  ${}_w\mathcal{F}$  frame.

### C. Boundedness and Convergence of the Wrench Estimator

In this section we comment on the stability of the force estimator which is critical for tactile-primitive selection. We prove that the estimate is bounded at all times and converges

to the arm-based estimate as  $t \rightarrow \infty$ . Let  $\hat{\delta}_{f_a} := \Upsilon \cdot \sum_{i=1}^4 \hat{\delta}_{f_i}$  denote the estimate from the spring-based arm wrench.

*Assumption 1:* Boundedness of estimated signals  $\hat{\delta}_{f_{CoM}}$  and  $\hat{\delta}_{f_a}$  and their derivatives  $\dot{\hat{\delta}}_{f_{CoM}}$ ,  $\dot{\hat{\delta}}_{f_a}$ . We assume that the individual estimates from the acceleration-based method employed on the UAV and the spring-damper arm are bounded.

*Remark 1:* Considering that most real-world estimators such as those proposed in [23] are employed for force feedback control, it is reasonable to assume that acceleration-based methods are bounded and provide bounded estimates even in the presence of uncertainties.

*Assumption 2:* The derivative of  $\dot{\hat{\delta}}_{f_{CoM}} \rightarrow 0$  as  $t \rightarrow \infty$ .

*Remark 2:* The acceleration-based estimator dynamics are second-order filter dynamics and hence it is assumed that the signal  $\dot{\hat{\delta}}_{f_{CoM}}$  converges to a bounded value implying the rate of change at the convergence is near zero.

*Proposition:* If  $\kappa_f$  is chosen such that  $\kappa_f = h(\dot{\hat{\delta}}_{f_{CoM}})$  where  $h(\cdot)$  is a function that continuously increases from 0 to 1 as the magnitude of  $\dot{\hat{\delta}}_{f_{CoM}}$  decreases, then  $\kappa_f \rightarrow 1$  if  $\dot{\hat{\delta}}_{f_{CoM}} \rightarrow 0$  and vice-versa. This allows for the estimate to be bounded at all times.

*Proof:* We now discuss the boundedness and convergence (steady state) of the proposed force estimator via a break-up into following three different stages.

- 1) *Steady-state phase:* From Assumption 2, at steady-state, the  $\dot{\hat{\delta}}_{f_{CoM}} \rightarrow 0$  and hence the proposed estimator will converge to the arm-based one, that is  $\hat{\delta}_f \rightarrow \hat{\delta}_{f_a}$ .
- 2) *Transient phase:* In the transient phase,  $\dot{\hat{\delta}}_{f_{CoM}} \rightarrow 1$  and hence the proposed estimator will converge to the CoM-based one, that is  $\hat{\delta}_f \rightarrow \hat{\delta}_{f_{CoM}}$ .
- 3) *Transition between transients and steady-state:* Finally by ensuring that  $h(\cdot) \in [0, 1]$  is a smooth function and from Assumptions 1 and 2, the force estimate from the proposed estimator is bounded at all times.

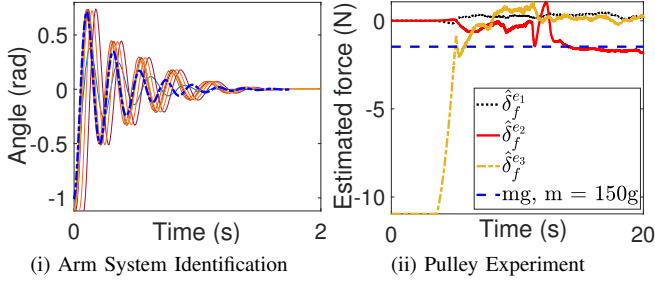


Fig. 9. (i) Arm dynamics characterization with a step input. The system identification is done in MATLAB to obtain the damping and spring coefficients. (ii) Validation of the proposed force estimator when there is no contact.

#### D. System Identification for Arm Dynamics

For the system identification of the arm dynamics, the inertia about  $z$ -axis for the arm,  $\mathcal{J}_{zz}$  was calculated using SolidWorks to be  $0.0015\text{kgm}^2$ . We design an experiment where the base of the XPLORER is held by a clamp and the torsional spring-based arm is first loaded to a certain fixed position using a force sensor. Then it is released and the motion capture system is used to record the trajectory of the arm (shown in Fig. 9i). We then use the MATLAB System ID toolbox to obtain the  $b$  and  $k$  values as 0.009 and 1.307 for values in Section III-A1.

#### E. Additional Results for Force Estimation at No Contact

In this section we present additional results for the pulley-mass experiment which is to show that when there is no contact, the estimator correctly relies on the CoM-based estimate and the interaction controller successfully uses these estimates to exert the desired force. A mass of 150g was attached to a pulley and directly anchored to the CoM of XPLORER. A desired force equal to weight of the test-mass was commanded. As shown by the results in Fig. 9ii, the proposed estimator successfully utilizes the CoM-based estimate to perform the task. The results were consistent over three trials for each of 100g, 150g and 200g test masses.

#### F. Algorithms

This section presents *Exploration*, *Tactile turning* and *Tactile-traversal* in an algorithmic format. The position and yaw reference before current time-step is denoted by  $[\mathbf{x}_{sp}^*(k) \ \psi^*(k)]^T$  and is used to reshape the reference at current step,  $[\mathbf{x}_{sp}(k) \ \psi(k)]^T$ . Furthermore, we transform the reference into the inertial frame whenever necessary via

$$[\mathbf{x}_{sp}^b \ y_{sp}^b \ z_{sp}^b]^T = {}_b^w \mathbf{R} [\mathbf{x}_{sp} \ y_{sp} \ z_{sp}]^T \quad (10)$$

where  $[\mathbf{x}_{sp}^b \ y_{sp}^b \ z_{sp}^b]$  denote the reference in the body frame,  ${}_b\mathcal{F}$ , and  $[\mathbf{x}_{sp} \ y_{sp} \ z_{sp}]$  denote them in inertial frame  ${}_w\mathcal{F}$ . Similarly, 10 is also used to calculate the current position in body frame,  $\mathbf{x}^b$ , from current position in inertial frame,  $\mathbf{x}$ .

*Note:* `AdmittanceController()` in Algorithms 1-3 refers to implementation of (7) from the main article which reshapes the position and yaw reference based on desired wrench.

#### G. Time-optimal control with state jumps

1) *Problem setup:* Consider the following double integrator dynamics for a continuous-time system with states  $\tilde{\mathbf{x}} \in \mathbb{R}^2$ :

$$\dot{\tilde{x}}_1 = \tilde{x}_2, \quad \dot{\tilde{x}}_2 = u \quad (11)$$

---

#### Algorithm 1: Exploration

---

**Input:**  $\mathbf{x}^b, [\mathbf{x}_{sp}^* \ \psi_{sp}^*]^T, \psi$  &  $\hat{\delta}_f^b$   
**Output:**  $[\mathbf{x}_{sp}^b \ \psi_{sp}]^T$  &  $\Gamma$   
**Parameters:**  $d_{step}$   
1 **if**  $|\psi| < \psi_o$  &  $|\hat{\delta}_f^b| < \delta_o$  **then**  
2      $\mathbf{x}_{sp}^b(k) = \mathbf{x}^b(k) + d_{step}$   
    $\mathbf{y}_{sp}^b(k) = (\mathbf{y}_{sp}^*)^b(k)$   
    $\psi_{sp}(k) = \psi_{sp}^*(k)$   
3 **else if**  $|\psi| > \psi_o$  **then**  
4      $\Gamma = 2$   
5 **else**  
6      $\Gamma = 3$

---

#### Algorithm 2: Tactile Turning

---

**Input:**  $[\mathbf{x}_{sp}^* \ \psi_{sp}^*]^T, \psi$  &  $\hat{\delta}_f^b$   
**Output:**  $[\mathbf{x}_{sp} \ \psi_{sp}]^T$  &  $\Gamma$   
**Parameters:**  $\mathcal{W}, dt$   
1 **if**  $|\psi| > \psi_o$  &  $|\hat{\delta}_f^b| < \delta_{\psi_o}$  **then**  
2      $\mathbf{x}_{sp}(k) = \mathbf{x}_{sp}^*(k)$   
    $\dot{\psi}_{sp}(k) = \text{sgn}(\psi) \mathcal{W} \cdot dt$   
3 **else**  
4      $\Gamma = 3$

---

It is assumed that the jump pattern is induced by the flow set  $\mathcal{C} := \{\tilde{\mathbf{x}} \in \mathbb{R}^2\}$  and the jump set which denotes the locations for collision is denoted by  $\mathcal{D} = \{\tilde{\mathbf{x}} \in \mathbb{R}^2 | \tilde{x}_1 = a, \tilde{x}_2 \leq 0\}$ . Here,  $a$  is the location of objects that XPLORER can collide on. Furthermore, let the hybrid system be described by:

$$\dot{\tilde{\mathbf{x}}} = \mathbf{A}\tilde{\mathbf{x}} + \mathbf{B}u \text{ if } \tilde{\mathbf{x}} \in \mathcal{C}, \tilde{\mathbf{x}}^+ = \mathbf{E}\tilde{\mathbf{x}} \text{ if } \tilde{\mathbf{x}} \in \mathcal{D} \quad (12)$$

where  $\mathbf{A} \in \mathbb{R}^{2 \times 2}$  is state matrix,  $\mathbf{B} \in \mathbb{R}^{2 \times 1}$  is input matrix and  $\mathbf{E} \in \mathbb{R}^{2 \times 2}$  denotes the state evolution during the jump.

The conventional time-optimal control for a system to reach  $(0, 0)$  from a state  $\tilde{\mathbf{x}}_0$  is given by the *bang-bang* control law where the control only takes the values  $\{-1, 1\}$  and at most one switch is required. More specifically, the trajectories are characterized by the family of the parabolas:

$$\begin{cases} u = +1 \\ \tilde{x}_1(t) = +\frac{1}{2}t^2 + \alpha t + \beta \\ \tilde{x}_2(t) = +t + \alpha \\ \tilde{x}_1 = \frac{1}{2}\tilde{x}_2^2 + \beta - \frac{\alpha^2}{2} \end{cases} \quad \begin{cases} u = -1 \\ \tilde{x}_1(t) = -\frac{1}{2}t^2 + \alpha t + \beta \\ \tilde{x}_2(t) = -t + \alpha \\ \tilde{x}_1 = -\frac{1}{2}\tilde{x}_2^2 + \beta - \frac{\alpha^2}{2} \end{cases}$$

with the switching curve  $\Pi := \{\tilde{\mathbf{x}} : \tilde{x}_1 + \frac{1}{2}\tilde{x}_2|\tilde{x}_2|\}$  and parameters  $\alpha, \beta$ . Furthermore, given the initial condition, the optimal time is given by:

$$t_0^*(\tilde{\mathbf{x}}_0) = \begin{cases} 2\sqrt{\frac{1}{2}\tilde{x}_{20}^2 + \tilde{x}_{10} + \tilde{x}_{20}}, \tilde{\mathbf{x}}_0 \in S^- \\ |\tilde{x}_{20}|, \tilde{\mathbf{x}}_0 \in \Pi \\ 2\sqrt{\frac{1}{2}\tilde{x}_{20}^2 - \tilde{x}_{10} - \tilde{x}_{20}}, \tilde{\mathbf{x}}_0 \in S^+ \end{cases} \quad (13)$$

where  $\mathbb{R}^2 = S^- \cup \Pi \cap S^+$ ,  $S^\pm$  stands for the regions below and above the switching curve  $\Pi$ .

2) *Time optimal control with 1 state jump due to collisions:* We now extend the analysis to study the case scenarios where collisions induce a state jump in velocity. For this case, let the jump map  $\mathbf{E}$  be given by

$$\mathbf{E} = \begin{bmatrix} 1 & 0 \\ 0 & e \end{bmatrix} \quad (14)$$

where  $e$  stands for the coefficient of post collision velocity as a function of the coefficient of restitution. This value  $e$  can be obtained using a linearization of the collision model in

**Algorithm 3:** Tactile Traversal

---

**Input:**  $x^b, \psi, [x_{sp}^* \ \psi_{sp}^*]^T$  &  $\hat{\delta}_f^b$  &  $\hat{\delta}_\tau^{e3}$   
**Output:**  $[x_{sp}^b \ \psi_{sp}^b]^T$  &  $\Gamma$   
**Parameters:**  $\delta_0, \delta_{f_{des}}$

```

1 Function CollisionNormal():
2   if  $\lambda = "+X"$  or  $"-X"$  then
3     if  $\hat{\delta}_f^{b1} > \delta_0$  then
4        $C_n = [1, 0, 0, 0]$ 
5     else if  $\hat{\delta}_f^{b1} < -\delta_0$  then
6        $C_n = [0, 1, 0, 0]$ 
7     else if  $\lambda = "+Y"$  or  $"-Y"$  then
8       if  $\hat{\delta}_f^{b2} > \delta_0$  then
9          $C_n = [0, 0, 1, 0]$ 
10      else if  $\hat{\delta}_f^{b2} < -\delta_0$  then
11         $C_n = [0, 0, 0, 1]$ 
12    return  $C_n$ 
13 Function MoveDirection():
14    $C_n \leftarrow$  ContactNormal()
15   if  $C_n == [1, 0, 0, 0]$  then
16      $\lambda = "+Y"$ 
17   else if  $C_n == [0, 1, 0, 0]$  then
18      $\lambda = "-Y"$ 
19   else if  $C_n == [0, 0, 1, 0]$  then
20      $\lambda = "-X"$ 
21   else if  $C_n == [0, 0, 0, 1]$  then
22      $\lambda = "+X"$ 
23   return  $\lambda$ 
24 Function TrajectoryGeneration():
25    $\lambda \leftarrow$  MoveDirection()
26    $\psi_{sp} = \psi_{sp}^*$ 
27   if  $\lambda = "+X"$  then
28      $x_{sp}^b(k) = x^b + d_{step}$ 
29      $\delta_{f_{des}} = [0 \ \Delta_{f_{des}} \ 0]^T, \delta_{\tau_{des}} = \hat{\delta}_\tau^{e3}$ 
30      $x_{sp}(k) =$  AdmittanceController( $\delta_{f_{des}}, \delta_{\tau_{des}}$ )
31   else if  $\lambda = "-X"$  then
32      $x_{sp}^b(k) = x^b - d_{step}$ 
33      $\delta_{f_{des}} = [0 \ -\Delta_{f_{des}} \ 0]^T, \delta_{\tau_{des}} = \hat{\delta}_\tau^{e3}$ 
34      $x_{sp}(k) =$  AdmittanceController( $\delta_{f_{des}}, \delta_{\tau_{des}}$ )
35   else if  $\lambda = "+Y"$  then
36      $y_{sp}^b(k) = y^b + d_{step}$ 
37      $\delta_{f_{des}} = [\Delta_{f_{des}} \ 0 \ 0]^T, \delta_{\tau_{des}} = \hat{\delta}_\tau^{e3}$ 
38      $x_{sp}(k) =$  AdmittanceController( $\delta_{f_{des}}, \delta_{\tau_{des}}$ )
39   else if  $\lambda = "-Y"$  then
40      $y_{sp}^b(k) = y^b - d_{step}$ 
41      $\delta_{f_{des}} = [-\Delta_{f_{des}} \ 0 \ 0]^T, \delta_{\tau_{des}} = \hat{\delta}_\tau^{e3}$ 
42      $x_{sp}(k) =$  AdmittanceController( $\delta_{f_{des}}, \delta_{\tau_{des}}$ )
43 Function Main():
44   CollisionNormal()
45   MoveDirection()
46   TrajectoryGeneration()

```

---

the Section -H. Then any generic point  $\tilde{z}$  on the jump set  $\mathcal{D}$  can be denoted by  $\tilde{z} = (a, \zeta)$  where  $a$  denotes the position of the wall and  $\zeta$  denotes the pre-collision velocity. The optimal path to  $\tilde{z}$  from any given initial point  $\tilde{x}_0$  are given by the two branches of parabolas with a switching curve passing through  $\tilde{z}$  as  $\Phi(\zeta) = \{\tilde{x} : \frac{1}{2}(\tilde{x}_2 + \zeta)|\tilde{x}_2 - \zeta| - a + \tilde{x}_1\}$ .

We can again decompose the state space as  $\mathbb{R}^2 = \Psi^- \cup \Phi \cap \Psi^+$  where  $\Psi^\pm$  is similarly defined as the regions below and above the switching curve  $\Phi$ . The optimal time taken to reach  $\tilde{z}$  from

**Algorithm 4:** Mapping Framework

---

**Input:**  $[x, y, z]^T, \psi, \hat{\delta}_f^b, C_n$  &  $\lambda$   
**Output:** Point Cloud Data  
**Parameters:**  $\delta_{map}$

```

1 if  $|\hat{\delta}_f^b| \geq \delta_{map}$  then
2   if  $\lambda(k-1) \neq \lambda(k)$  then
3      $\lfloor$  Add Corner Block to Point Cloud
4   else
5      $\lfloor$  Add Obstacle to Point Cloud in  $C_n$  axis
6 else
7    $\lfloor$  Store Point Cloud Data

```

---

$\tilde{x}_0$  can then be written as:

$$\tau(\tilde{x}_0, \zeta) = \begin{cases} \left| \zeta + \sqrt{\frac{\zeta^2}{2} + \frac{\tilde{x}_{20}^2}{2} - a + \tilde{x}_{10}} \right| + \tilde{x}_{20} \\ + \sqrt{\frac{\zeta^2}{2} + \frac{\tilde{x}_{20}^2}{2} - a + \tilde{x}_{10}}, & \tilde{x}_0 \in \Psi^+(\zeta), \\ \left| \tilde{x}_{20} - \zeta \right|, & \tilde{x}_0 \in \Phi(\zeta), \\ \left| \zeta - \sqrt{\frac{\zeta^2}{2} + \frac{\tilde{x}_{20}^2}{2} + a - \tilde{x}_{10}} \right| - \tilde{x}_{20} \\ + \sqrt{\frac{\zeta^2}{2} + \frac{\tilde{x}_{20}^2}{2} + a - \tilde{x}_{10}}, & \tilde{x}_0 \in \Psi^-(\zeta) \end{cases} \quad (15)$$

The corresponding optimal control law is given as:

$$u_1^* = \begin{cases} 1, & \text{if } j = 0, \gamma_0(\tilde{x}(t, 0)) < 0 \\ -1, & \text{if } j = 0, \gamma_0(\tilde{x}(t, 0)) > 0 \\ -\text{sgn}(\tilde{x}_2(t, 0) - z_2^*(\tilde{x}_0)), & \text{if } j = 0, \gamma_0(\tilde{x}(t, 0)) = 0 \\ 1, & \text{if } j = 1, \gamma_1(\tilde{x}(t, 1)) < 0 \\ -1, & \text{if } j = 1, \gamma_1(\tilde{x}(t, 1)) > 0 \\ -\text{sgn}(\tilde{x}_2(t, 1)), & \text{if } j = 1, \gamma_1(\tilde{x}(t, 1)) = 0 \end{cases} \quad (16)$$

where the functions  $\gamma_0 : \mathbb{R}^2 \rightarrow \mathbb{R}$  and  $\gamma_1 : \mathbb{R}^2 \rightarrow \mathbb{R}$  are:

$$\gamma_0(\tilde{x}) = \frac{1}{2}(\tilde{x}_2 + z_2^*(\tilde{x}_0))|\tilde{x}_2 - z_2^*(\tilde{x}_0)| - z_1^*(\tilde{x}_0) + \tilde{x}_1$$

$$\gamma_1(\tilde{x}) = \tilde{x}_1 + \frac{1}{2}\tilde{x}_2|\tilde{x}_2|$$

Furthermore, the 1-jump minimum time is given by

$$t_1^*(\tilde{x}_0) = \min_u \{\tau(\tilde{x}_0, \zeta) + t_0^*(E\tilde{z})\} \quad (17)$$

where  $E\tilde{z}$  denotes the post collision state. The proof follows [44]. We use this result to motivate and introduce *Ricocheting*.

*Remark 3:* For our experiments, we only select ricocheting if the collision-based travel time—calculated as the time to reach the collision node at maximum velocity plus the time from the post-collision velocity to the goal—is shorter than a direct flight under P-PID control. We begin by choosing the maximum velocity XPLORER can attain (from a discrete set) in the closed flight space and verify via the CollisionNet that a reduced rebound state is indeed generated post-collision. Intuitively,  $\zeta$  is both upper- and lower-bounded: it must not be so large that traveling to the collision node inflates total maneuvering time, nor so small that it prematurely diverts the UAV from its course. We will derive these bounds formally in our future work.

3) *Illustrative example for time-optimal state jumps:* In this subsection we present an example to motivate *Ricocheting*. For this case, we assume the coefficient of restitution  $e = -0.6$  in (14) and a wall at  $a = 0.5$ . The UAV starts from an initial state  $\tilde{x}_0 = [-1 \ 2]^T$ , marked by a diamond in Fig. 5 right.

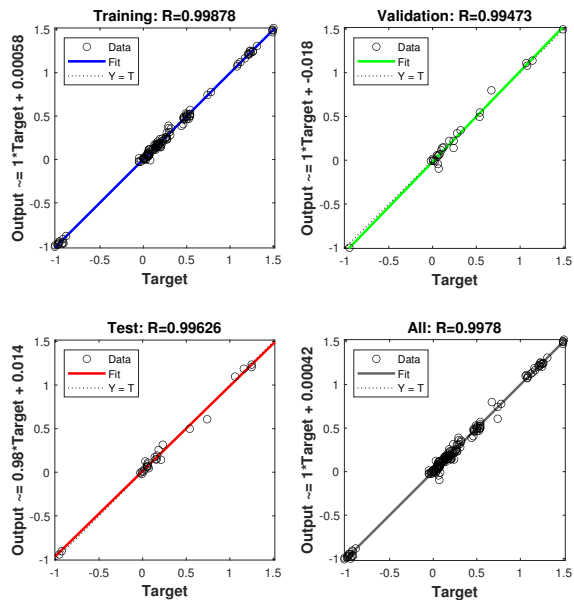


Fig. 10. Validation results for the collision neural network showing the  $R^2$  values obtained for the trained model. We see that the trained network is able to predict the post collision state with high accuracy.

For a double integrator system, the right-open parabolic curves represent trajectories under maximum control,  $\tilde{u} = 1$  while the left-open curves correspond to minimum control  $\tilde{u} = -1$ . The bang-bang control law (without collisions) achieves minimum-time travel in 4 seconds, following the red-magenta trajectory (1-4-5) in Fig. 5 right, where deceleration continues until the trajectory intersects the switching curve (magenta), followed by acceleration to reach (0,0).

For the collision-inclusive path, a state  $(a, \zeta)$  after collision translates to  $(a, -e\zeta)$ . Using (15), the minimum time to reach (0,0) via collision and maximum deceleration is 1.756 seconds, with  $\zeta^* = 1.667$  and  $e = 0.6$ . The corresponding bang-bang-jump-bang trajectory is shown by the path 1-2-3-4-5, blue-magenta curved lines, in Fig. 5 right.

In summary for lower values of  $e$ , as is the case for deformable quadrotors, *Ricocheting* off an edge near the stopping node will produce a minimum time path for efficient braking.

#### H. CollisionNet- A Neural Network for post-collision state

From the set of 60 experiments, a data-driven collision model was developed to study the effects of collisions at various intensities and various angle of incidence for XPLOER. The experimental data collected are plotted as the pre-collision and post-collision velocities in Fig. 5 left of main article. This collision model is crucial to identify the coefficient of restitution and predict the post-collision state of the vehicle. Since the collisions for the deformable vehicle are highly nonlinear, a nonlinear regression model using neural networks was employed to develop the collision model- CollisionNet. MATLAB Deep Learning Toolbox (MATLAB R2021b) was employed for the training using Levenberg-Marquardt method. Five features were identified to train the model: the  $v_x^-, v_y^-$  representing pre-collision state, angle of incidence to the collision plane, and type of collision. The angle of incidence is a function of the orientation of the vehicle, while the type

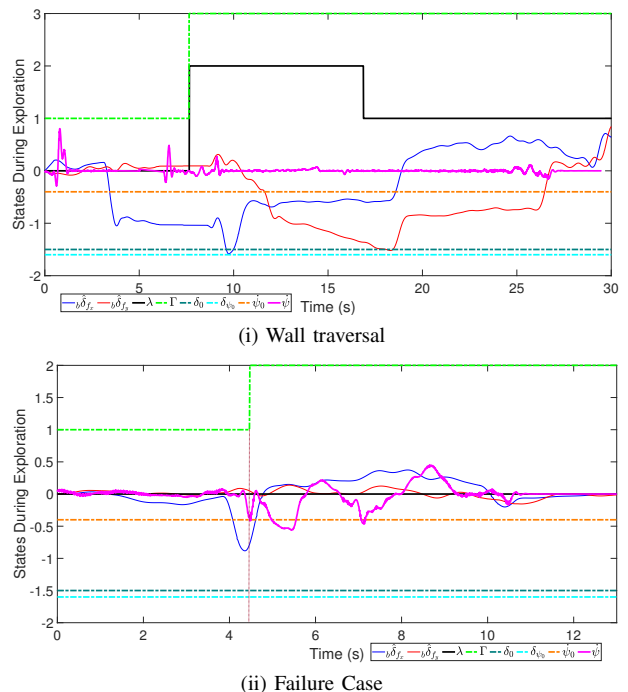


Fig. 11. Exploration results for rigid UAV. (a) For a wall-like structure, the performance is as desired, and  $\Gamma = 1, 3$  are engaged. (b) failures case when the yaw-torque at initial contact is high leading to engaging the *Tactile-turning* state with  $\Gamma = 2$  and failing to start the exploration scheme with  $\Gamma = 3$  that is *Tactile-traversal*.

of collision is either collide-to-stop (inelastic collision) or collide-to-decelerate (elastic collision). We choose 75% of the dataset for training and 25% for validation. The results for the CollisionNet are given in Fig. 10 and we see that the accuracy is very high with a  $R^2$  value of 0.99.

It is noticed from Fig. 5 that for different angles and same pre-collision state, the post collision state is always very similar for the 2D case. This shows that for this particular quadrotor design, angle of collision is not a critical parameter to model and hence justifies our assumption to use a point-mass based double integrator model to ricochet.

#### I. Additional results for rigid quadrotor

In this section we present additional results for exploration experiments with a rigid quadrotor of the same dimensions by deploying the exploration scheme developed for XPLOER. We conducted both wall-traversal and the box-traversal experiments out of which only the wall-traversal succeeded.

For the wall traversal results shown in Fig. 11i, the rigid UAV takes off and upon making initial contact, applies the desired force on the wall and initiates the *Tactile-traversal*. When it detects the second wall, it engages the traversal motion in the body +Y direction as shown by the black line.

Finally, another unpredictable behavior was observed with the rigid UAV, as shown in Fig. 11ii. Sometimes when the rigid UAV makes impact, due to the high rebound velocities, and the presence of yaw admittance control given by (7), there is a high yaw-rate which falsely triggers the *Tactile-turning* and the entire exploration fails. However this behavior is not observed with the XPLOER due to the damping effect and shock-absorbing nature of the torsion spring in the arm.